Published in IET Electric Power Applications
Received on 8th January 2014
Revised on 25th May 2014
Accepted on 13th June 2014
doi: 10.1049/iet-epa.2014.0005

ISSN 1751-8660

Design and iron loss analysis of sensorless-controlled interior permanent magnet synchronous motors with concentrated winding

Myung-Seop Lim, Seung-Hee Chai, Jung-Pyo Hong

Department of Automotive Engineering, Hanyang University, Seongdong-gu, Seoul 133-791, Republic of Korea
E-mail: hongjp@hanyang.ac.kr

Abstract: This study investigates the influence of the stator configuration of low-speed sensorless-controlled interior permanent magnet synchronous motors (IPMSMs) with concentrated winding on the sensorless drive feasibility and iron loss. To evaluate the sensorless controllability of the motors, a mathematical and simulation process of estimating the rotor position error is proposed. In addition, the harmonic iron loss under a load condition is analysed via two-dimensional non-linear finite element analysis. Considering both the sensorless drive feasibility and iron loss, the four different IPMSMs, which have different tooth tip configurations in the stator, are examined. It is shown that the machine with a relatively short and thin stator tooth tip has better sensorless drive controllability and lower harmonic iron loss than the others. Based on the analysis result, a final model applied with stator chamfer for electric vehicle traction is proposed and manufactured. The validity of the simulations and the design method are verified by the experiments.

1 Introduction

To save fossil fuel and prevent further global warming, there is currently a high demand for the development of vehicles using an electrical propulsion system, such as hybrid electric vehicles and electric vehicles. Especially, the interior permanent magnet synchronous motors (IPMSMs) are generally being employed for traction application [1]. This is because they have higher torque density and efficiency per unit rotor volume than other types of motors by utilising the magnetic and reluctance torque, and a wide operating speed range can be obtained with the help of field weakening control [2]. Meanwhile, to increase the reliability of vector-controlled IPMSMs, sensorless drive can be used. This means that the position sensors, such as the encoder and resolver, are replaced by an estimator, avoiding the cost of a position sensor and the increase of the system volume and complexity. Furthermore, the sensors are not durable enough to operate normally under severe environmental conditions in vehicles. This concern is coming to the fore because if the position sensors are in default, the driver cannot control the vehicle, which will result in an accident. Therefore a sensorless driving technique and a design method for sensorless-controlled motors are critical goals not only for system cost and volume reduction but also for fault-tolerant control feasibility.

At a high speed, a good estimation of the rotor position can be obtained by measuring the speed-dependent back electromotive force (BEMF) of the machine. This cannot be used in the zero- and low-speed ranges, however, because the magnitude of BEMF is extremely small. Thus, based on saliency, the rotor position can be estimated by measuring the current response or variation of the inductance with high-frequency voltage injection [3–5]. It is not easy to estimate the rotor position under heavy load conditions, although, because the responses are distorted by the input current or the cross-saturation [6–8]. This problem becomes more apparent when concentrated winding is applied to a motor [9], but there are only a few design methods using the q-axis path optimisation of the rotor [10–12]. It is hard to find prior researches on design methods using the geometry design parameters in the stator, considering both sensorless controllability and iron losses. Below are the advantages of applying the geometry design parameters to a stator compared with a rotor.

- There is no need to repeatedly conduct rotor stress analysis when the design parameters are applied to a stator.
- When there is a manufactured reference machine, the cost of and time needed to obtain and fabricate permanent magnets can be reduced because the rotor of the reference machine can be used as it is.

In this paper, the cause of the occurrence of the estimation error is discussed. As a result, the error can be simply predicted by evaluating the total harmonic distortion (THD) of the phase inductances and the contour plot of the d, q-axis mutual-inductance varied with the rotor position caused by the harmonics of the phase inductance [12]. Based on the error evaluation process, the influence of the design parameters in the stator on the sensorless control feasibility is analysed using finite element analysis (FEA).

The iron losses under the load conditions are also investigated using FEA because the performance of the IPMSMs can be seriously limited by the iron losses at a high speed. Thus, the goal of this study was to propose the design method for concentrated winding sensorless-oriented machines that can achieve excellent sensorless drive performances and minimise the iron loss.

2 Evaluation of the saliency-based sensorless drive feasibility

2.1 Basic principle of rotor position estimation

Rotor-saliency-based sensorless control is feasible by means of the high-frequency signal injection method. If the voltage injection angle is 0° when the voltage is injected into the d-axis, the d-axis self-inductance will have the minimum value, as shown in Fig. 1. Then the middle position of the permanent magnet (PM), which is the d-axis, can be estimated by sensing the minimum point of the d-axis self-inductance L_d or the zero-crossing of the d, q-axis mutual-inductance L_{dq} [8, 13]. The inductance waveforms, however, are distorted with the rotor position by the saturation of the core or by the cross-saturation effect. Thus, a particular simulation process has to be carried out as described in Fig. 2 to find the estimated rotor position error. First, FEA is conducted, including PMs. At this step, non-linear FEA has to be done to consider the saturation of the core under the load conditions. The next stage involves fixing the permeability at each mesh decided in the first step, converting the residual induction of the PM to 0, and performing linear FEA by applying the unit current to the coil of a single phase. Here, as for the magnet permeability, 1.05 was used, based on the PM material data used in the study. Then the self- and mutual-inductances can be obtained as linkage flux per unit current. At the fourth step, the procedure is iterated with the rotor position for one period in the electrical angle. Then the d, q-axis self- and mutual-inductances can be calculated via axis transformation. Finally, the contour plot of the d, q-axis mutual-inductance as an estimated rotor position error is obtained [9, 12].

2.2 Inductance harmonics and estimation error

The three-phase inductance matrix including harmonics obtained via FEA can be transformed into the d, q-axis inductance matrix using (1) [14]. The d, q-axis inductances varied with the rotor position contain the information about the estimated rotor position error. Thus, the mathematical process of figuring out the cause of the error is described as follows

$$L_{dq}^{r} = \frac{3}{2} T_{\theta_r} T_{dq} L_{abc} \left(T_{\theta_r} T_{dq} \right)^{\mathrm{T}} \tag{1}$$

where L_{abc} is the three-phase inductance matrix including harmonics; T_{dq} and $T_{\theta r}$ are the d, q-axis transform and rotational transform coefficients, respectively; and L_d, L_q, L_{dq} and L_{qd} are the d- and q-axis self- and mutual-inductances.

Whereas various harmonic wave components are mixed with the fundamental wave in actual inductance, to determine how the individual harmonic wave components in the phase inductance affect sensorless position estimation errors, it is necessary to mathematically model each harmonic wave model. Each harmonic term of the phase inductances, $L_{abc\mathrm{h}}$, is expressed mathematically as (2) to analytically determine the effect of the nth phase inductance harmonics on the d, q-axis inductances [13, 14]. n is the harmonic order of the phase inductances, and L_{h} is an unknown value, as the magnitude of the nth harmonic. $L_{abc\mathrm{h}}$ can be transformed into d, q-axis inductances.

$$L_{abc\mathrm{h}} = L_{\mathrm{h}} \begin{bmatrix} \cos 2\theta_r n & \cos 2n\left(\theta_r - \frac{\pi}{3}\right) & \cos 2n\left(\theta_r + \frac{\pi}{3}\right) \\ \cos 2n\left(\theta_r - \frac{\pi}{3}\right) & \cos 2n\left(\theta_r + \frac{\pi}{3}\right) & \cos 2\theta_r n \\ \cos 2n\left(\theta_r + \frac{\pi}{3}\right) & \cos 2\theta_r n & \cos 2n\left(\theta_r - \frac{\pi}{3}\right) \end{bmatrix} \tag{2}$$

The d, q-axis inductance caused by the nth harmonic of the

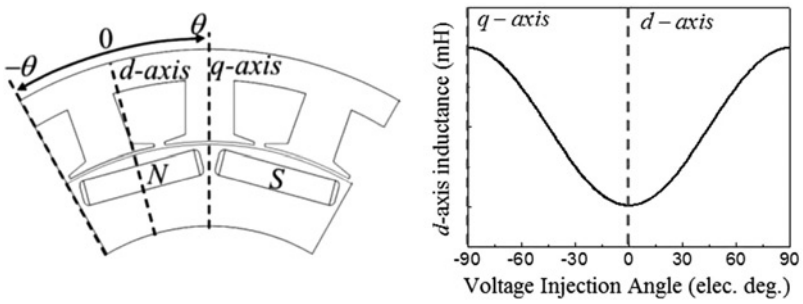

Fig. 1 *d-Axis inductance waveform with high-frequency voltage injection*

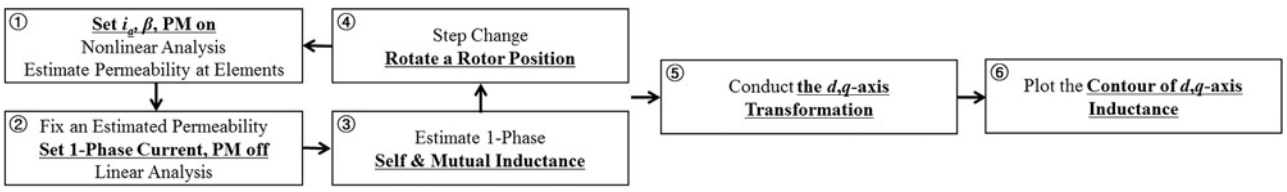

Fig. 2 *Flowchart of the simulation process of rotor position error estimation*

doi: 10.1049/iet-epa.2014.0005

Table 1 Relation between the harmonic orders of the phase inductances and the *d*,*q*-axis mutual-inductances

n	2	4	5	7	8	10	11	13	14	…
m	1	1	2	2	3	3	4	4	5	…
L_{dqh}	6	6	12	12	18	18	24	24	30	6 *k*-th

phase inductance can be obtained using (1) and (2)

$$L^r_{dqh} = \frac{3}{2}L_h\begin{bmatrix}\cos 6\theta_r m & -\sin 6\theta_r m\\ -\sin 6\theta_r m & -\cos 6\theta_r m\end{bmatrix} \quad \text{at} \quad n = 3m-1$$
$$L^r_{dqh} = \frac{3}{2}L_h\begin{bmatrix}\cos 6\theta_r m & \sin 6\theta_r m\\ \sin 6\theta_r m & -\cos 6\theta_r m\end{bmatrix} \quad \text{at} \quad n = 3m+1$$
$$L^r_{dqh} = 0 \quad \text{at} \quad n = 3m \tag{3}$$

where m is a natural number. As described in (3), the harmonics of the phase inductances, except the 3*k*th harmonic terms, cause the 6*k*th periodic ripple of the *d*, *q*-axis inductances varied with the rotor position during one period in the electrical angle ($k = 1, 2, 3,\ldots$). The relation between the harmonics of the phase inductances and the *d*, *q*-axis inductances can be organised simply as shown in Table 1. Therefore the magnitude of the estimation error is represented as well by examining the THD of the phase inductances, except the 3*k*th harmonic terms. Thus, in this paper, the THD excluding the 3*k*th harmonic waves of self-inductance among the phase inductance components, is proposed as a simple method of evaluating the accuracy of rotor position estimation, and is presented as THD_L.

3 Influence of the geometry design parameters in the stator

3.1 Sensorless drive feasibility

In this paper, the configuration of the stator tooth tip is analysed to determine their effects on the sensorless-oriented motors using non-linear two-dimensional (2D) FEA as the process, as shown in Fig. 2. Below are the assumptions and considerations for conducting FEA.

The input current is a sinusoidal wave.
The diameters of the conductors should be small enough to neglect the skin effect [15].
The eddy current loss in the PM is neglected.
The magnetic resistance and lamination effect are considered in the material data (flux density against magnetomotive force and iron loss against frequency data).
The full load condition of the machines in the paper is 115 Nm–14 kW at a rated speed of 1160 rpm.

Four IPMSMs with different tooth tip configurations are illustrated in Fig. 3: model 1 (short and thin), model 2 (long and thin), model 3 (short and thick) and model 4 (long and thick). The tooth tip dimensions of slot open L_{so} and the thickness of the tooth tip end T_{te} of the models are organised in Table 2. The self-inductance L_a varied with the rotor position and THD_L, and the estimation errors under the full load conditions are shown in Fig. 4 to evaluate the sensorless drive feasibility. As for finding the estimation error in Fig. 4, the phase inductance waveforms found using FEA were converted using (1), and a contour plot for *d*, *q*-axis mutual-inductance L_{dq} was plotted. An examination of the results shows that the THD_L and angle estimation error are proportional. It was found that model 1 is the most suitable design for the sensorless drive because of its minimum error. In conclusion, the shape of the tooth tip is one of the critical design factors for sensorless drive machines. Furthermore, it can be expected that geometry parameters that have an influence on the saturation of the tooth tip, such as the chamfer and notch in the stator, can be used to design sensorless-oriented, concentrated-winding IPMSMs.

3.2 Losses

In particular, IPMSMs are appreciated for their good efficiency and large speed ranges because of their flux weakening capability, provided that the motor is suitably designed for such aim. At a high speed, however, the performance of the IPMSMs can be seriously limited by the

Table 2 Dimension of the tooth tip and BEMF of the four models

	Slot open, L_{so}, mm	Thickness of the tooth tip end, T_{te}, mm	Phase BEMF at 1000 rpm, V_{rms}
model 1	6	1.53	41.17
model 2	3	1.31	40.77
model 3	6	2.51	41.69
model 4	3	2.28	41.41

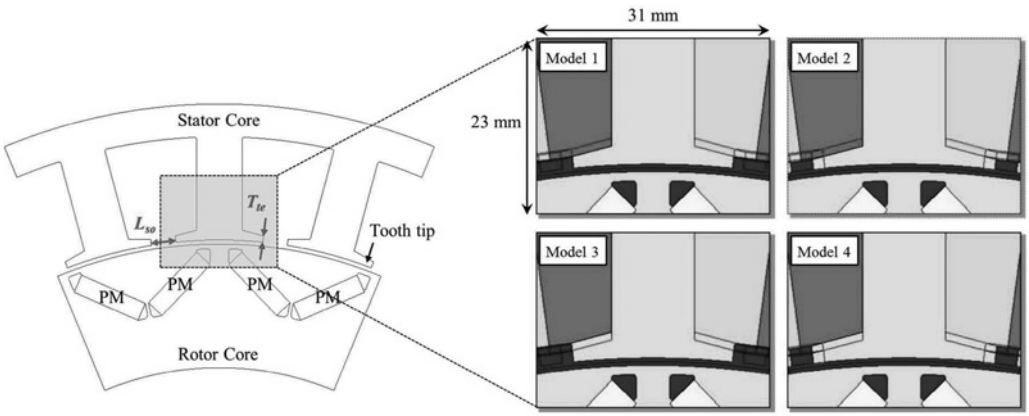

Fig. 3 *Different tooth tip configurations in the four IPMSMs*

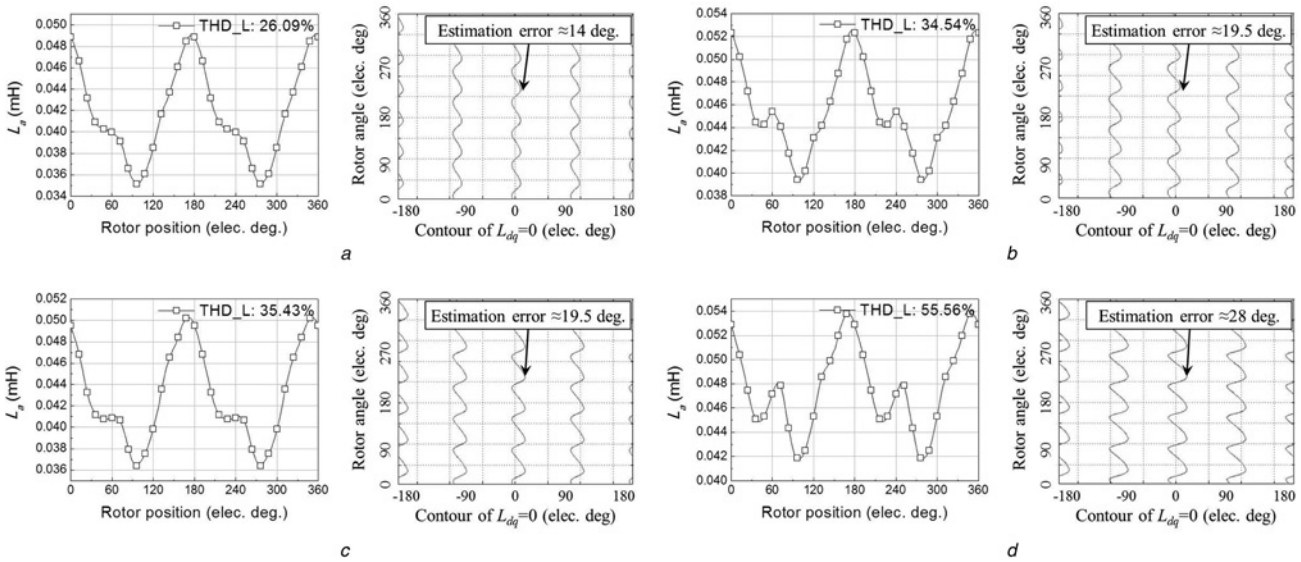

Fig. 4 *One-phase self-inductances L_a varied with the rotor position, and the estimation error*

a Model 1
b Model 2
c Model 3
d Model 4

iron losses [16]. Thus, the iron losses under the load conditions should be analysed to evaluate the feasibility of the proposed design method because the method is related to the saturation of the stator tooth tip, which means that the proposed method is closely related to the iron loss. Fig. 5 shows the process of determining the iron losses [17, 18].

Step 1: Using non-linear FEA, the flux density at each mesh for one electrical angle period is calculated, as the rotor is rotated under a load condition. Here, the flux density is calculated as the normal and tangential components.
Step 2: Using the flux density from step 1, Fourier transform is performed to find the magnitude of the fundamental and harmonic components.
Step 3: From the iron loss data for the material, the iron loss corresponding to the frequency and flux density of each harmonic is calculated. The material information is based on the empirical data.
Step 4: The sum of the iron loss because of the harmonic components at each mesh is calculated.
Step 5: The iron losses of all the meshes are added to determine the total iron loss of the machine.

Given the results of the analysis, as shown in Figs. 6*a* and *b*, the iron loss of the machine is generally affected by the size of the tooth tip rather than by the saturation levels in the tooth tips of the models. It can be noted that as the speed rises, a higher operating frequency magnifies the difference in iron loss among the models. The copper losses of the models determined by the magnitude and phase of the input current are shown in Fig. 6*c*. The total losses shown in Fig. 6*d* were determined considering the mechanical, copper and iron losses. The mechanical losses of the models were analytically calculated using the equation in [19]. The mechanical losses were the same because the motors had the same rotor diameters. In a low-speed region, model 1 had a lower total loss than the others. In a high-speed region, model 1 had a larger copper loss but a smaller iron loss than the others. In conclusion, whereas the iron loss for model 1, which had the smallest tooth tip, was significantly smaller, because of copper loss, the total loss reduction was negligible. The efficiencies at the maximum speed (6560 rpm) were found to be as follows: model 1, 89.10%; model 2, 89.05%; model 3, 89.04%; and model 4, 88.96%. Therefore, for the final improved model proposed in this paper, chamfers were applied to the stator as a design

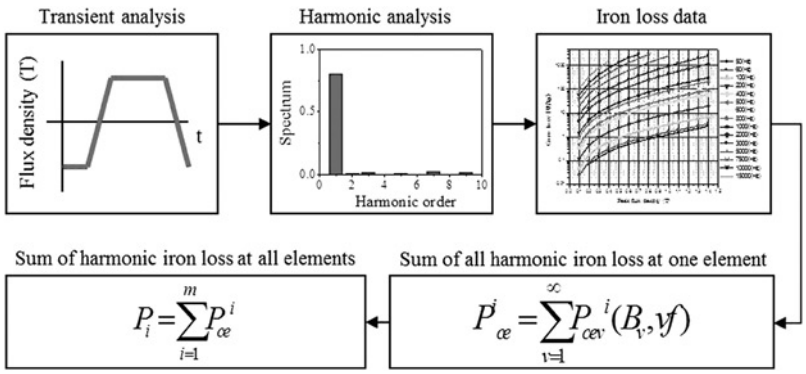

Fig. 5 *Process of calculating the iron losses*

doi: 10.1049/iet-epa.2014.0005

element to minimise the estimation error, and reduce not only the iron loss but also the total loss.

4 Improved model

4.1 Design results of the improved model

To reduce the cross-sectional area of the tooth tip and to facilitate saturation, the improved model was added chamfers on the tooth tip. Its cross-section is presented in Fig. 7, and the parameters of the improved model are listed in Table 3. The d, q-axis inductances and the estimated rotor position error under the full load condition are shown in Fig. 8. Given the simulation result, the maximum estimation error of the improved model is about 11.5° in the electrical angle under the full load condition. The error of the improved model is smaller than the errors of the four models proposed above. Besides, it is expected that the error will not be over 11.5° under any load condition because it is possible that the steady-state angle error can be reduced by means of the compensation algorithm.

In addition, in Figs. 9*a* and *b*, the losses for the improved model and for model 1 which had the lowest iron and total losses among the four previous models, are compared. It is shown that the total loss of the improved model is smaller than those of the previous models shown in Fig. 6 because of the low iron loss in the high-speed region. It can be seen that improved model has lower iron loss and total loss and the difference in the losses also increases as the speed increases. Figs. 9*c* and *d* separately show the results of the

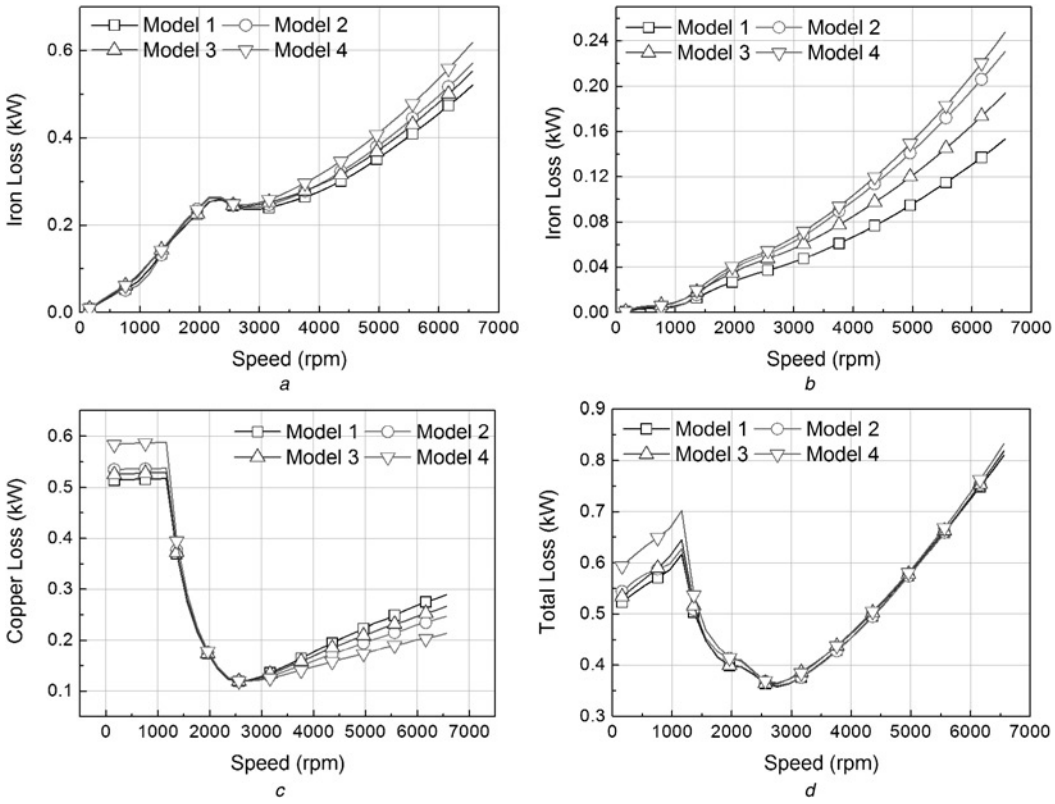

Fig. 6 *Losses under the 115 Nm–14 kW load conditions of the models (0–1160 rpm: maximum torque per ampere control; 1160–6560 rpm: flux weakening control)*

a Iron loss
b Iron loss in the tooth tip of the models
c Copper loss
d Total loss

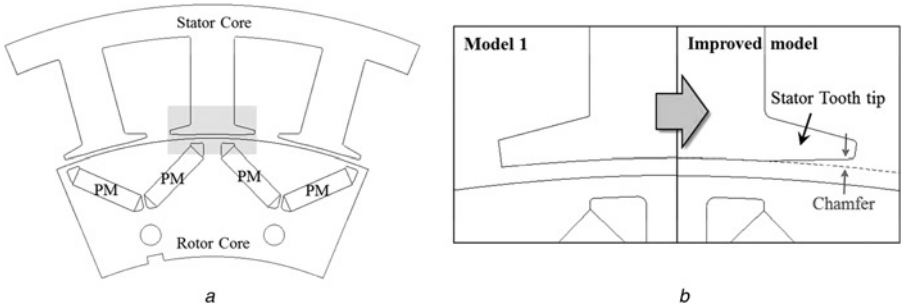

Fig. 7 *Configuration of the improved model*

a Cross-section of the improved model
b Comparison of the tooth tip of the improved model with that of model 1

Table 3 Parameters of the improved model

	Improved model, unit
maximum power	14 kW
maximum torque	115 Nm
base/maximum speed	1160/6560 rpm
pole/slot	16/24
winding	Concentrated winding
slot open	6 mm
thickness of tooth tip end	1 mm
phase back EMF	40.65 V_{rms}
DC-link voltage	320 V
phase resistance	15.97 mΩ

analysis of the iron losses and the loss per unit volume of each part in the improved model. The iron loss in the tooth tip rapidly increases at higher speed as shown in Fig. 9*c*. The iron loss per unit volume in the tooth tip was found to have been the greatest as shown in Fig. 9*d*. Thus, minimising the iron loss in the tooth tip is important to minimise the total iron loss of the machine, as the proposed design method in the paper. In conclusion, the improved model with better sensorless drive characteristics and lower iron loss than the four models was achieved in this study through the proposed design procedure using the stator chamfer with the short and thin tooth tip.

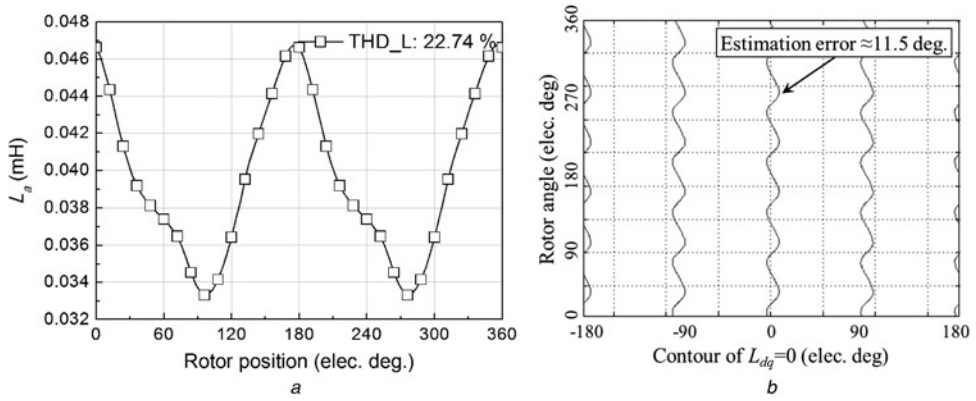

Fig. 8 *L_a waveform and estimation error of the improved model*

a Self-inductance
b Estimation error

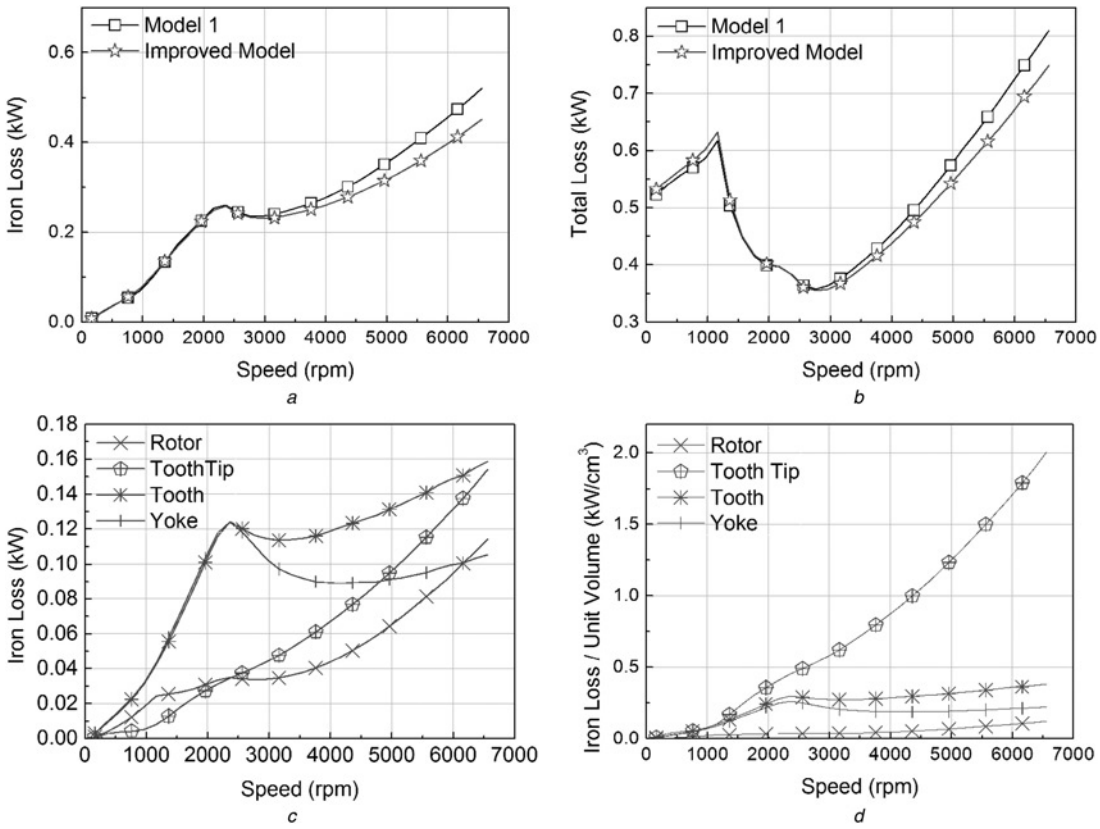

Fig. 9 *Iron and total loss of the improved model under the full load conditions*

a Iron loss compared to the model 1
b Total loss compared to the model 1
c Iron loss of each part in the improved model
d Iron loss per unit volume of each part in the improved model

doi: 10.1049/iet-epa.2014.0005

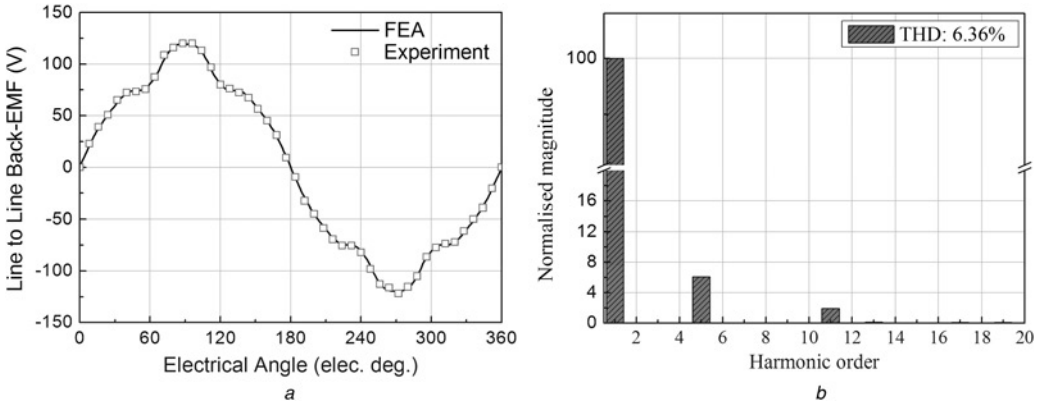

Fig. 10 *Line-to-line BEMF waveforms and THD of the improved model at 1000 rpm*

a Line-to-line BEMF at 1000 rpm
b FFT of the line-to-line BEMF

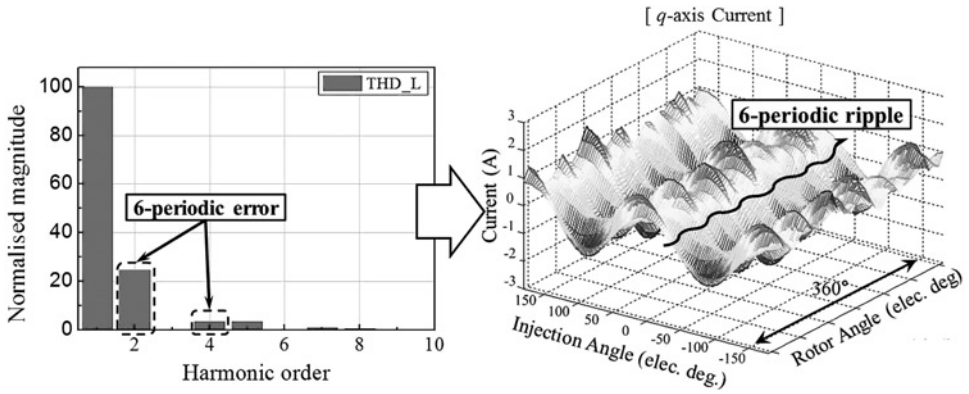

Fig. 11 *Sixth current ripple as an experiment result caused by the phase inductance harmonics*

Table 4 Position error at the steady state of the improved model

Speed, rpm	*q*-axis current				
	140 A	98 A	0 A	−98 A	−140 A
0	−1.3°	1.3°	0.9°	0.7°	0.9°
200	−1.3°	0.4°	1.9°	1.0°	−1.1°

4.2 Validation of FEA and the design process

The improved model was tested to verify the validity of the simulations. A load machine, a torque sensor and the test motor were connected mechanically in series in the experiment setup. The machine was operated using a pulse-width modulation inverter, whose switching frequency was 16.5 kHz in the load test. The line-to-line BEMF at 1000 rpm under the no-load condition obtained via non-linear 2D FEA and through an experiment are compared in Fig. 10. The error of the BEMF between FEA and the experiment results was only 1.6%. The THD of the line-to-line BEMF was 6.36%. It affected the electrical characteristics of the machine, but it can be considered a minor factor for the traction application in this paper. This is because the traction motor is directly connected to the high mechanical inertias in a traction system. Fig. 11 shows

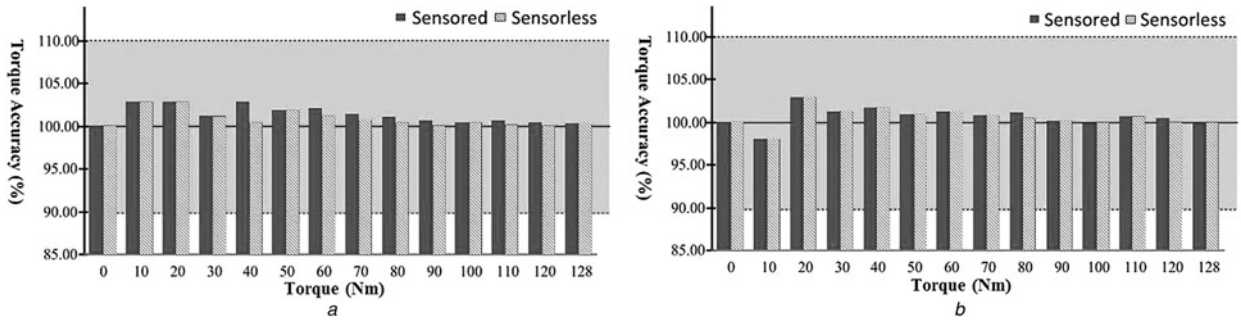

Fig. 12 *Torque accuracy test results*

a 100 rpm
b 200 rpm

the fast Fourier transform (FFT) result of L_a and the current response obtained in the experiment under the full load condition. The 6-periodic ripple was mainly caused by the second and fourth harmonics of L_a, as described in Section 2.2. Table 4 shows that the rotor position estimation errors were experimentally determined about 0.9°–1.9° at 0 and 200 rpm. To verify the validation of the design process presented in this paper, Fig. 12 shows the torque test results of a sensored and a sensorless drive at 100 and 200 rpm, respectively. The discrepancies between the torque accuracies are not over 2.5%, and the torque accuracy is almost 100% in all the desired torque operations. In conclusion, the improved model achieved excellent sensorless drive performance through the proposed design method.

5 Conclusion

The design method of the concentrated-winding IPMSM for sensorless control at a low speed including standstill was investigated in this study. The estimation method of the rotor position error was determined through the analytic and simulation process. Using the estimation methods, the geometry design parameters in a stator were analysed. As a result, it was found that the configuration of the stator tooth tip is a critical factor. In particular, small cross-sectional area of the stator tooth tip generally has a positive effect on both the sensorless drive characteristics and the iron loss under the load conditions. Based on the analysis results, the improved model was proposed and tested. The validity of the simulations and design method was verified through an experiment. Therefore it can be concluded that the proposed design method is useful for achieving great sensorless controllability and for minimising the iron loss for designing a saliency-based sensorless-controlled IPMSM with concentrated winding.

6 Acknowledgment

This research was supported by the MKE (The Ministry of Knowledge Economy), Korea, under the CITRC (Convergence Information Technology Research Center) support program (NIPA-2013-H0401–13-1008) supervised by the NIPA (National IT Industry Promotion Agency).

7 References

1 Laskaris, K.I., Kladas, A.G.: 'Internal permanent magnet motor design for electric vehicle drive', *IEEE Trans. Ind. Electron.*, 2010, **57**, (1), pp. 138–145

2 Chau, K.T., Chan, C.C., Liu, C.: 'Overview of permanent-magnet brushless drive for electric and hybrid electric vehicles', *IEEE Trans. Ind. Electron.*, 2008, **55**, (6), pp. 2246–2257

3 Sayeef, S., Foo, G., Rahman, M.F.: 'Rotor position and speed estimation of a variable structure direct-torque-controlled IPM synchronous motor drive at very low speeds including standstill', *IEEE Trans. Ind. Electron.*, 2010, **57**, (11), pp. 3715–3723

4 Caruana, C., Asher, G.M., Bradley, K.J., Woolfson, M.: 'Flux position estimation in cage induction machines using synchronous HF injection and Kalman filtering', *IEEE Trans. Ind. Appl.*, 2003, **39**, (5), pp. 1372–1378

5 Corley, M.J., Lorenz, R.D.: 'Rotor position and velocity estimation for a salient-pole permanent magnet synchronous machine at standstill and high speeds', *IEEE Trans. Ind. Appl.*, 1998, **34**, (4), pp. 784–789

6 Kano, Y., Kosaka, T., Matsui, N., Fujitsuna, M.: 'Sensorless-oriented design of concentrated winding IPM motors for HEV drive application'. Int. Conf. Electrical Machines, Marseille, France, September 2012, pp. 2709–2715

7 Li, Y., Zhu, Z.Q., Howe, D., Bingham, C.M.: 'Modeling of cross-coupling magnetic saturation in signal-injection-based sensorless control of permanent-magnet brushless AC motors', *IEEE Trans. Magn.*, 2007, **43**, (6), pp. 2552–2554

8 Zhu, Z.Q., Li, Y., Howe, D., Bingham, C.M.: 'Compensation for rotor position estimation error due to cross-coupling magnetic saturation in signal injection based sensorless control of PM brushless AC motor'. Int. Conf. Electric Machines and Drives, Antalya, Turkey, May 2007, pp. 208–213

9 Kano, Y., Kosaka, T., Matsui, N., Nakanishi, T.: 'Design and experimental verification of a sensorless-oriented concentrated-winding IPMSM'. Int. Conf. Electrical Machines, Rome, Italy, September 2010, pp. 1–6

10 Bianchi, N., Bolognani, S.: 'Influence of rotor geometry of an IPM motor on sensorless control feasibility', *IEEE Trans. Ind. Appl.*, 2007, **43**, (1), pp. 87–96

11 Wrobel, R., Budden, A.S., Salt, D., *et al.*: 'Rotor design for sensorless position estimation in permanent-magnet machines', *IEEE Trans. Ind. Electron.*, 2011, **58**, (9), pp. 3815–3824

12 Sergeant, P., De Belie, F., Melkebeek, J.: 'Rotor geometry design of interior PMSMs with and without flux barriers for more accurate sensorless control', *IEEE Trans. Ind. Electron.*, 2012, **59**, (6), pp. 2457–2465

13 Chai, S.H., Lee, B.H., Hong, J.P., Sul, S.K., Kim, S.M.: 'Design of IPMSM having high power density for position sensorless operation with high-frequency signal injection and the method of calculating inductance profile'. Int. Conf. Electrical Machines and Systems, Beijing, China, August 2011, pp. 1–5

14 Matsui, N., Takeda, Y., Morimoto, S., Honda, Y.: 'Design and control of IPMSM' (Ohmsha Ltd., 2001)

15 Hanselman, D.C., Peake, W.H.: 'Eddy-current effects in slot-bound conductors', *IEE Proc. Electr. Power Appl.*, 1995, **142**, (2), pp. 131–136

16 Pellegrino, G., Guglielmi, P., Vagati, A., Villata, F.: 'Core losses and torque ripple in IPM machines: dedicated modeling and design tradeoff', *IEEE Trans. Ind. Appl.*, 2010, **46**, (6), pp. 2381–2391

17 Lee, B.H., Kwon, S.O., Sun, T., Hong, J.P., Lee, G.H., Hur, J.: 'Modeling of core loss resistance for *d-q* equivalent circuit analysis of IPMSM considering harmonic linkage flux', *IEEE Trans. Magn.*, 2011, **47**, (5), pp. 1066–1069

18 Kang, G.H., Hong, J.P., Kim, G.T., Park, J.W.: 'Improved parameters modeling of interior permanent magnet synchronous motor based on finite element analysis', *IEEE Trans. Magn.*, 2000, **36**, (4), pp. 1867–1870

19 Takeuchi, T.: 'Electric machine design' (Ohmsha Ltd., 1979)

doi: 10.1049/iet-epa.2014.0005